










# Optimization of radiochromic film stacks to diagnose high-flux laser-accelerated proton beams

Cite as: Rev. Sci. Instrum. **91**, 093303 (2020); <https://doi.org/10.1063/5.0020568>

Submitted: 01 July 2020 . Accepted: 26 August 2020 . Published Online: 17 September 2020

C. B. Curry , C. A. S. Dunning , M. Gauthier , H.-G. J. Chou , F. Fiuza , G. D. Glenn , Y. Y. Tsui , M. Bazalova-Carter , and S. H. Glenzer 



View Online



Export Citation



CrossMark

## ARTICLES YOU MAY BE INTERESTED IN

[Development of fluorescence-yield wavelength-dispersive x-ray absorption spectroscopy in the soft x-ray region for time-resolved experiments](#)



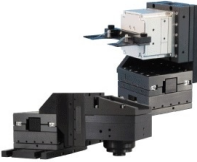
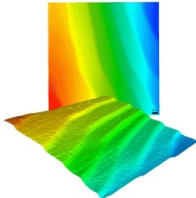
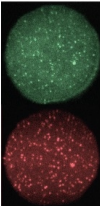
Review of Scientific Instruments **91**, 093104 (2020); <https://doi.org/10.1063/5.0021981>

[Ion species discrimination method by linear energy transfer measurement in Fujifilm BAS-SR imaging plate](#)

Review of Scientific Instruments **91**, 093305 (2020); <https://doi.org/10.1063/5.0016515>

[Broad-beam plasma-cathode electron beam source based on a cathodic arc for beam generation over a wide pulse-width range](#)

Review of Scientific Instruments **91**, 093304 (2020); <https://doi.org/10.1063/5.0023172>

 <b>MCL</b> MAD CITY LABS INC. <a href="http://www.madcitylabs.com">www.madcitylabs.com</a>	<p>Nanopositioning Systems</p> 	<p>Modular Motion Control</p> 	<p>AFM and NSOM Instruments</p> 	<p>Single Molecule Microscopes</p> 
---	--	--	---	--

# Optimization of radiochromic film stacks to diagnose high-flux laser-accelerated proton beams

Cite as: Rev. Sci. Instrum. 91, 093303 (2020); doi: 10.1063/5.0020568

Submitted: 1 July 2020 • Accepted: 26 August 2020 •

Published Online: 17 September 2020



C. B. Curry,<sup>1,2,a)</sup> C. A. S. Dunning,<sup>3,4</sup> M. Gauthier,<sup>1</sup> H.-G. J. Chou,<sup>1,5</sup> F. Fiuza,<sup>1</sup> G. D. Glenn,<sup>1,6</sup> Y. Y. Tsui,<sup>2</sup> M. Bazalova-Carter,<sup>3,4</sup> and S. H. Glenzer<sup>1</sup>

## AFFILIATIONS

<sup>1</sup>High Energy Density Science Division, SLAC National Accelerator Laboratory, Menlo Park, California 94025, USA

<sup>2</sup>Department of Electrical and Computer Engineering, University of Alberta, Edmonton, Alberta T6G 1H9, Canada

<sup>3</sup>Department of Physics and Astronomy, University of Victoria, Victoria, British Columbia V8P 5C2, Canada

<sup>4</sup>BC Cancer, Provincial Health Services Authority, Victoria, British Columbia V8R 6V5, Canada

<sup>5</sup>Physics Department, Stanford University, Stanford, California 94305, USA

<sup>6</sup>Applied Physics Department, Stanford University, Stanford, California 94305, USA

<sup>a)</sup>Author to whom correspondence should be addressed: [ccurry@slac.stanford.edu](mailto:ccurry@slac.stanford.edu)

## ABSTRACT

Here, we extend flatbed scanner calibrations of GafChromic EBT3, MD-V3, and HD-V2 radiochromic films using high-precision x-ray irradiation and monoenergetic proton bombardment. By computing a visibility parameter based on fractional errors, optimal dose ranges and transitions between film types are identified. The visibility analysis is used to design an ideal radiochromic film stack for the proton energy spectrum expected from the interaction of a petawatt laser with a cryogenic hydrogen jet target.

Published under license by AIP Publishing. <https://doi.org/10.1063/5.0020568>

## I. INTRODUCTION

Ion acceleration from high-intensity laser–plasma interactions has attracted great interest due to potential applications ranging from fast ignition inertial confinement fusion<sup>1,2</sup> to precision tumor treatment with proton therapy.<sup>3–5</sup> Recently, research in ultra-high dose rate (FLASH) proton radiotherapy ( $\geq 40$  Gy/s), such as those readily obtained with laser-accelerated proton beams, has been rekindled after a significant reduction in toxicity to healthy surrounding tissues was observed post-treatment.<sup>6,7</sup> While these applications have yet to be fully realized, laser-accelerated proton beams have been widely used in high-energy-density science experiments for proton radiographic imaging of laser-produced plasmas,<sup>8,9</sup> stopping power measurements,<sup>10,11</sup> and to produce isochorically heated warm dense matter.<sup>12–14</sup>

Proton radiography has arguably been the most successful application of laser-driven proton beams to date. The laminarity, apparent divergence from a micrometer-sized virtual source

point, and broad energy bandwidth (1 MeV–85 MeV) make proton beams accelerated by the Target Normal Sheath Acceleration (TNSA) mechanism well suited for probing electric and magnetic fields that are tens of micrometers in size and evolving on the picosecond timescale.<sup>15</sup> If the proton beam diverges for tens of millimeters before probing an electric or magnetic field, a geometric magnification of the interaction is obtained; however, the temporal dispersion of the ion beam can exceed  $\sim 100$  ps. A spatially and energy resolving detector, such as a radiochromic film stack,<sup>16–21</sup> is then required for picosecond resolution snapshots of fast-evolving fields occurring in high-intensity laser–plasma interactions.

Several radiochromic film (RCF) types exist with different dose sensitivities. A “stack” of RCF consisting of multiple film types is routinely used to collect energy-resolved measurements. Ion energy measurements made with RCF exploit the characteristic energy deposition curve of a ballistic ion through matter, commonly referred to as the Bragg curve. When a projectile ion travels through a cold material, the velocity,  $v$ , decreases after successive inelastic

collisions with bound electrons. Due to the large difference in mass between the ion and electrons, the initial ion trajectory is unaffected until the ion energy is comparable to that of bound electrons in the cold material. As the ion slows, the interaction cross section, also referred to as the stopping power, increases proportionally to  $1/v^2$ . A detector consisting of successive layers of radiation-sensitive films can be used to measure the energy profile of an ion beam determined only by the stack thickness. To increase the energy separation between successive layers, metallic filters can be added. This becomes particularly important to design a large-energy-range stack that provides a high dynamic range.

In this work, we present the calibrations of GafChromic (Ashland, Covington, KY) EBT3, MD-V3, and HD-V2 films with a primary focus on calibration uncertainty to optimize the RCF stack for use as a quantitative diagnostic in petawatt laser-driven proton acceleration experiments.

## II. DOSE DEPOSITION IN RADIOCHROMIC FILM

Radiochromic films are designed for 2D dosimetry measurements of x rays, electrons, ions, and neutron beams. Upon exposure to ionizing radiation, the dye in the active layer of the film darkens as a function of the deposited dose. GafChromic EBT3, MD-V3, and HD-V2 cover low to high dose ranges, respectively. Unlike other detectors (e.g., ionization chambers), radiochromic films are believed to have a dose-rate independent response. An experiment performed at the Next Linear Collider Test Accelerator (NLCTA) at the SLAC National Accelerator Laboratory demonstrated dose-rate independence up to  $9 \times 10^{12}$  Gy/s.<sup>22</sup> Here, we use high-precision x-ray irradiation to accurately resolve the initial increase in optical density and then a 2D Gaussian monoenergetic proton beam to attain higher doses, thereby extending the calibrations into the saturation regime. Note that MD-V3 films were not included in the proton measurements.

**TABLE I.** Summary of linear accelerator outputs (Gy/min) on the four different shifts of irradiation for each of the three different treatment setups depicted in Figs. 1(a)–1(c).

	Standard	Normalized	Shortened-SSD
Shift 1	5.100	5.940	48.384
Shift 2	N/A	6.090	46.272
Shift 3	N/A	6.090	46.272
Shift 4	N/A	5.982	45.000

### A. High-precision x-ray irradiation

Three different setups were used during the x-ray film irradiations adapted for the total intended dose: standard, normalized, and shortened-source-to-surface distance (shortened-SSD) with 10 MV photon beams from a Truebeam linear accelerator (Varian Medical Systems, Palo Alto, CA) at BC Cancer—Victoria. A schematic of each setup is shown in Fig. 1. The films were placed in a rectangular phantom consisting of solid water slabs (CIRS, Norfolk, VA) at a setup-dependent depth described below. In each setup, a 5 cm slab was placed below the films to provide a sufficient backscatter. In each of the three different treatment field setups, the collimator jaws were set to produce a  $10 \times 10$  cm<sup>2</sup> field at the isocenter of the linear accelerator at 100 cm from the source. The output of the linear accelerator was determined with an N30013 model Farmer ionization chamber (PTW, Freiburg, Germany) with the chamber placed in the location of the film based on the AAPM TG 51 protocol.<sup>23</sup> The output of the linear accelerator, which differed by shift and configuration, is summarized in Table I.

In the standard setup, the films were placed at 10 cm depth in the phantom at 90 cm SSD. In the normalized setup, the films were placed at 2.2 cm depth, the depth of maximum dose for 10 MV photons at a SSD of 97.8 cm. For both of these setups, a flattening filter mode with a dose rate of 600 Monitor Units per minute (MU/min)

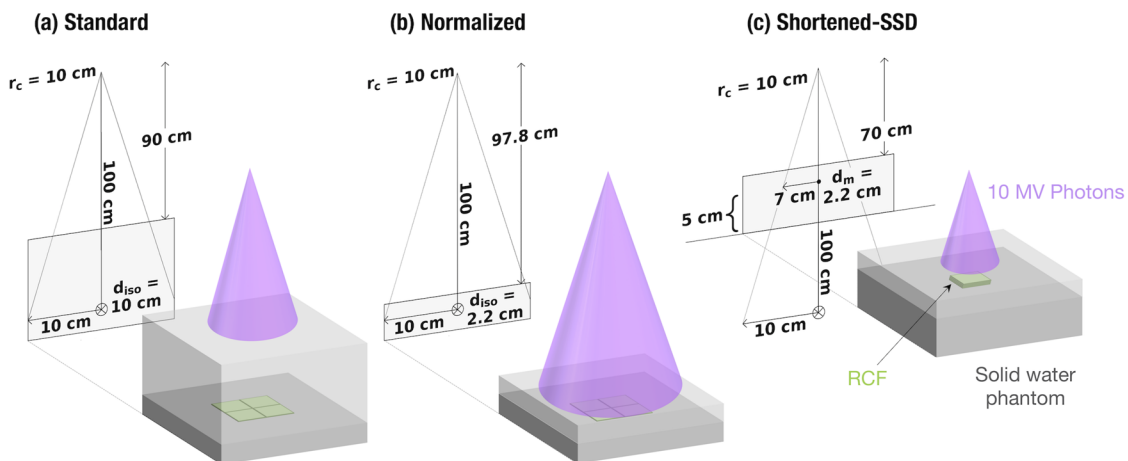


**FIG. 1.** (a) Standard treatment setup with 90 cm SSD and isocenter at a depth ( $d_{iso}$ ) of 10 cm. The flattening filter was used. (b) Normalized treatment setup with 97.8 cm SSD and isocenter at 2.2 cm depth, which is the depth of the maximum dose for 10 MV photons. The flattening filter was used. (c) Shortened-SSD treatment setup with 70 cm SSD with films placed a depth ( $d_m$ ) of 2.2 cm, which is the depth of the maximum dose for 10 MV photons. No flattening filter was used. The gray shaded region represents solid water slabs in all three configurations. RCF was irradiated in a  $2 \times 2$  grid (standard, normalized) or stack of four (shortened-SSD) as depicted by the green squares.

was used that resulted in a flat beam profile to allow for simultaneous irradiation of four films arranged in a  $2 \times 2$  grid. These irradiation setups were suitable for delivering low and medium doses between 0.1 Gy and 255 Gy to the EBT3 and MD-V3 films.

In the shortened-SSD setup, the films were placed at a depth of 2.2 cm at an SSD of 70 cm, which is the shortest distance within the geometrical constraints of the linear accelerator. While the reduced-SSD setup doubled the output of the linear accelerator, allowing faster dose delivery, the field size at the film location was reduced to  $7 \times 7$  cm<sup>2</sup>. The flattening filter was removed in this setup, which quadrupled the dose rate from 600 MU/min to 2400 MU/min using the 10 MV flattening filter free (FFF) mode. The combined effect of the reduced SSD and the removed flattening filter increased the irradiation rate eightfold, which is more suitable for delivering high doses of between 125 Gy and 2000 Gy to the MD-V3 and HD-V2 films. The removal of the flattening filter resulted in a Gaussian beam profile that is flat to within 3% standard deviation in the 2 cm central beam area, which just covered one film. Four films were stacked and irradiated together. Even if the four films were all the thicker MD-V3 film, this stacking would reduce the dose in the bottom film by at most 0.4% due to the film thickness of 260  $\mu$ m.

## B. Monoenergetic proton bombardment

Complementary measurements were performed with monoenergetic protons from the TR24 cyclotron located at the Medical Isotope and Cyclotron Facility (MICF, University of Alberta). The proton beam energy and approximate charge were calculated from the activation of natural copper foils placed behind the radiochromic films. The nuclear activity of the copper after proton irradiation was measured using a high purity germanium (HPGe) high resolution gamma spectrometer. Using the ratio of the  $^{nat}\text{Cu}(p, x)^{62}\text{Zn}$  and  $^{nat}\text{Cu}(p, x)^{63}\text{Zn}$  reaction probabilities, the incident proton energy can be precisely determined. The proton energy in the active layer of the HD-V2 ( $18.0 \pm 0.3$  MeV) and EBT3 ( $17.2 \pm 0.3$  MeV) films was inferred using the continuous slow-down approximation (CSDA). The proton stopping powers from the NIST PSTAR database combined with the proton charge computed from the total copper activity are used to estimate the dose. Major sources of error on the absolute charge arise from the gamma counting statistics, uncertainty in the HPGe detector efficiency, and nuclear activation cross sections. More details about the setup and methods can be found in Ref. 24.

## III. EXTENDED-RANGE RADIOCHROMIC FILM CALIBRATIONS

After exposure, all radiochromic films were placed in a light-tight box to develop for at least 48 h. They were then scanned with an Epson Perfection V750 Pro flatbed scanner in transmission mode.<sup>25</sup> Both 16-bit gray scale and 48-bit red-green-blue (RGB) images were recorded with a resolution of 300 dots per inch (dpi). For each film type and batch, a reference (non-irradiated) film was stored in the same conditions and used to remove background dose accumulation over time, film aging, and batch-to-batch variability. The change in optical density (OD) as a function of dose was then computed

directly from the exposed and reference films according to

$$\Delta OD = OD - OD_0 = -\log_{10}\left(\frac{C_{exp}}{C_{ref}}\right), \quad (1)$$

where  $C_{exp}$  and  $C_{ref}$  are the transmitted signals in counts for the exposed and reference film, respectively.<sup>26</sup> The OD of the films irradiated by x rays was measured by averaging across the entire film, excluding a narrow border around the edges and visible irregularities due to dust or scratches on the film.

Monoenergetic protons, on the other hand, were delivered with a Gaussian, radially symmetric dose profile resulting from a 0.5 mm pinhole located 237 mm from the films. A normalized dose profile was obtained from the EBT3 film with the lowest deposited dose, which had the full range of OD covered by the x-ray calibration. Benefiting from the overlapping dose ranges provided by the Gaussian distribution, the absolute dose in subsequent films was iteratively determined from low to high dose. The same procedure was performed for HD-V2. In both cases, the more-precise normalized dose profile from EBT3 could be used since the separation between the films was negligible. For clarity, only the maximum dose and the corresponding  $1\sigma$  variation resulting from the iterative technique are shown in the calibration figures.

Numerous calibrations of HD-V2 have been conducted in recent years.<sup>27–29</sup> Bin *et al.*<sup>29</sup> showed that calibrations can be extended to very high doses exploiting the high stopping power of low energy protons (i.e., 1.06 MeV); however, the dose must have a linear energy transfer (LET) correction applied to account for a decrease in film response near the Bragg peak due to ionization along the proton trajectory.<sup>30</sup> In addition, the total uncertainty in the calibration and the scanner response function, which were not taken into account in the study, may limit its usable dose range. Alternatively, Feng *et al.*<sup>24</sup> developed an advanced scanning technique using a monochromatic (e.g., 468 nm) pixel-by-pixel transmission scanner that can extend the usable range upward of 25 kGy. Despite this, conventional flatbed scanners remain the most common method to digitize the radiochromic film. Here, we use a combination of precision x-ray irradiation and monoenergetic proton bombardment to determine a robust calibration and focus specifically on optimal dose ranges based on the total uncertainty.

The resulting calibration for HD-V2 is shown in Fig. 2. The inset in Fig. 2 shows the very high dose behavior of the optical density. A saturation plateau is clearly identified above  $\sim 10$  kGy. We tested the manufacturer's suggested model for the functional dependence between OD and dose but found that the data for all three film types were better fit to second- or third-order rational functions with positive fitting coefficients. The resulting fits for the red and green channels of HD-V2 are given by

$$\Delta OD_{R, HD-V2}(d) = \frac{1.288d^3 + 5097d^2 + 6.543d \times 10^6}{d^3 + 4018d^2 + (1.049d + 266.6) \times 10^7}, \quad (2)$$

$$\Delta OD_{G, HD-V2}(d) = \frac{1.475d^3 + 10530d^2 + 6.308d \times 10^7}{d^3 + 7492d^2 + (8.571d + 7775) \times 10^7}, \quad (3)$$

where  $\Delta OD_R$  and  $\Delta OD_G$  are the change in optical density computed from Eq. (1) for the red and green channels, respectively, and  $d$  is the dose in gray.

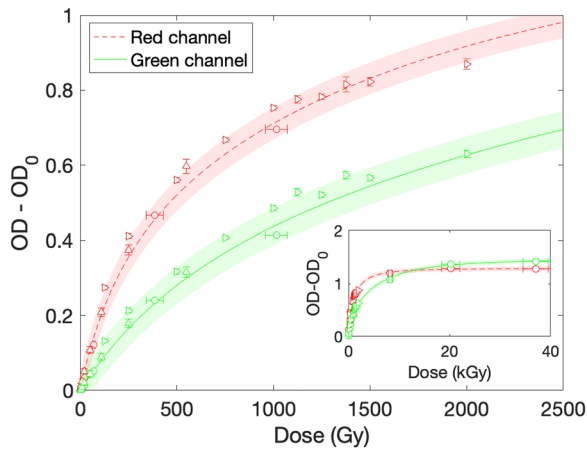


**FIG. 2.** Calibration of HD-V2 using an Epson Perfection V750 Pro flatbed scanner in transmission mode. Data consist of x-ray irradiation (right pointing triangles), 18.0 MeV monoenergetic proton bombardment (circles), and measurements by Chen *et al.*<sup>27</sup> (up pointing triangles) using the same x-ray irradiation methodology as Sec. II A. Inset: saturation behavior of HD-V2.

In the case of MD-V3 (Fig. 3), both the red and green channels provide a high quality calibration curve over the range of 10 Gy–1000 Gy. At low doses, the red channel is more responsive but begins to plateau near 180 Gy. Above these doses, the green channel should be used. Both channels reach saturation at ~1000 Gy. The calibration curves for MD-V3 are given by

$$\Delta OD_{R,MD-V3}(d) = \frac{0.8162d^2 + 42.41d}{d^2 + 156.1d^2 + 2394}, \quad (4)$$

$$\Delta OD_{G,MD-V3}(d) = \frac{0.7846d^2 + 18.33d}{d^2 + 165.6d^2 + 1678}. \quad (5)$$

Finally, EBT3 calibrations (Fig. 4) were extended from the previously published values<sup>27,31–33</sup> up to ~1000 Gy. The red channel is

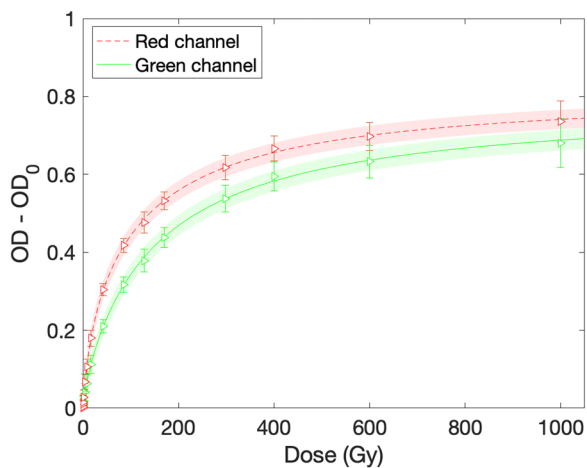


**FIG. 3.** Calibration of MD-V3 using an Epson Perfection V750 Pro flatbed scanner in transmission mode. All measurements performed with x-ray irradiation.

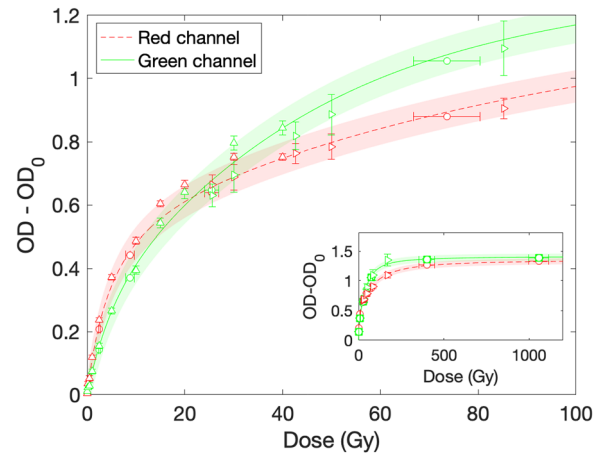


**FIG. 4.** Calibration of EBT3 using an Epson Perfection V750 Pro flatbed scanner in transmission mode. Data consist of x-ray irradiation (right pointing triangles), 17.2 MeV monoenergetic proton bombardment (circles), and measurements by Chen *et al.*<sup>27</sup> (up pointing triangles) using the same x-ray irradiation methodology as Sec. II A. Inset: saturation behavior of EBT3.

more sensitive at low doses. A saturation plateau is identified at ~200 Gy. The fits for the red and green channels of EBT3 are given by

$$\Delta OD_{R,EBT3}(d) = \frac{1.362d^3 + 75.26d^2 + 7247d}{d^3 + 82.22d^2 + 10310d + 57680}, \quad (6)$$

$$\Delta OD_{G,EBT3}(d) = \frac{1.416d^3 + 7.699d^2 + 1969d}{d^3 + 17.48d^2 + 2432d + 26180}. \quad (7)$$

#### IV. DIAGNOSIS OF HIGH-FLUX ION BEAMS FROM PETAWATT-CLASS LASERS

Recently, higher conversion efficiency ion acceleration mechanisms have been demonstrated using high-energy lasers with pulse durations ranging from 1 ps to 10 ps.<sup>34</sup> In particular, recent experiments utilizing the 1.5 kJ Advanced Radiographic Capability (ARC) laser at the National Ignition Facility have demonstrated proton fluxes on the order of  $10^{13}$  protons/MeV/sr.<sup>35</sup> With improvements to beam focusability using hemispherical targets,<sup>13</sup> multi-beam synchronization, and laser pulse contrast, it is ultimately expected that proton beams with fluxes exceeding  $10^{14}$  protons/MeV/sr will be produced.

Since RCF remains the preferred detector for high dynamic range, large-angle measurements of laser-accelerated proton beams, it is important to quantify the dose-dependent error due to the film calibrations and the read-out method. Using this, the stack design can be optimized to yield high visibility measurements at experimentally relevant energies. Although calibrations have been extended well above the manufacturer's recommended dose range, the uncertainty in dose and computed incident particle flux increases exponentially as the films saturate. To assess this effect quantitatively, we can define a dose-dependent visibility for each film type



according to

$$V(d) = 1 - \max\left(\frac{s\epsilon_{OD}}{df'(d)}, \frac{\epsilon_d(d, \epsilon_{OD})}{d}\right), \quad (8)$$

where  $s$ ,  $\epsilon_{OD}$ ,  $d$ , and  $f'(d)$  are the minimum signal-to-noise ratio, the average  $1\sigma$  variation in optical density from the scanner used, the dose in gray, and the first derivative of optical density with respect to dose from the calibration.  $\epsilon_d$  is the error in dose computed numerically by convolving the  $1\sigma$  error in the calibration with the  $1\sigma$  uncertainty in optical density from the scanner. For our case, we set the minimum signal-to-noise ratio to 2 and found that  $\epsilon_{OD}$  was 0.01. The first term in the maximum only considers the error resulting from background noise on the scanner, important at low doses when the films have small changes in OD. Once the OD is several times the scanner noise, the uncertainty in the calibration curve, included with the second term, becomes dominant. Note that a visibility less than or equal to zero represents a  $>100\%$  uncertainty in the absolute computed dose even if a change in OD is detected.

The computed visibility curves based on the calibration for the green channel of HD-V2, MD-V3, and EBT3 are shown in Fig. 5. This metric makes it clear that it is necessary to include a film sensitive to intermediate dose levels, such as MD-V3, in order to resolve a broadband source such as a semi-Maxwellian TNSA proton energy distribution. In addition, it is clearly evident that the visibility drops rapidly and far below the maximum calibrated values of HD-V2 to date. In order to maximize the visibility across the RCF stack, the transition from EBT3 to MD-V3 and MD-V3 to HD-V2 should occur at 71.45 Gy and 580.7 Gy, respectively.

Using this formalism, we can design an RCF stack that is optimized for laser-driven ion acceleration with a petawatt laser. Here, we use a proton energy spectrum from a 2-dimensional (2-D) particle-in-cell simulation performed using OSIRIS<sup>36</sup> for a  $1\ \mu\text{m}$  thick planar cryogenic hydrogen jet<sup>37,38</sup> irradiated at normal incidence by the Texas Petawatt laser (135J, 135 fs, and  $\sim 10^{21}\ \text{W/cm}^2$ ). The resulting proton energy spectrum, measured in the 2D simulation normal to the target surface, was corrected for 3D effects

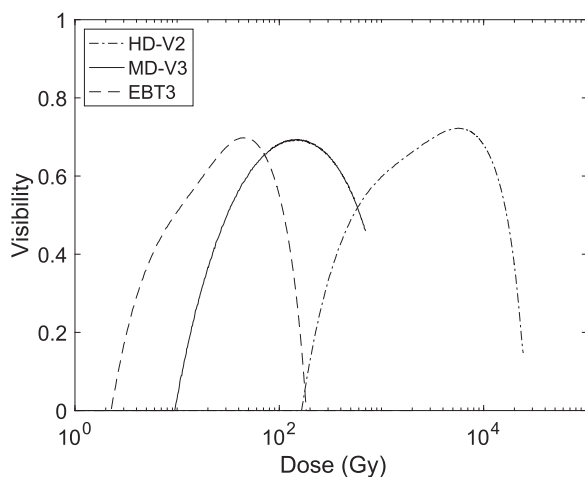


**FIG. 5.** Visibility as a function of dose computed from Eq. (8) for the green channel calibration of EBT3 (dashed), MD-V3 (solid), and HD-V2 (dotted-dashed).

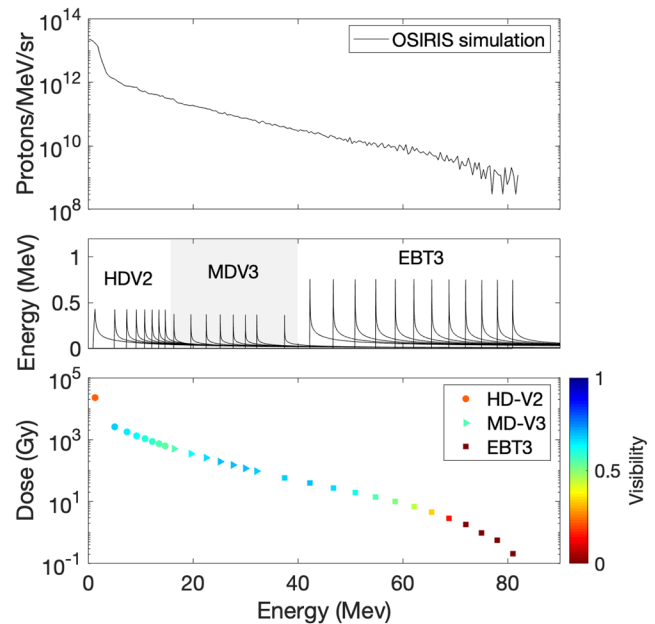


**FIG. 6.** Top: proton energy spectrum obtained from a 2D PIC simulation of a solid-density  $1\ \mu\text{m}$  thick planar hydrogen target irradiated by a high-energy petawatt laser. The proton energy was scaled down by a factor of 3 to correct for the impact of 3D effects on reducing the maximum energy. Middle: radiochromic film stack design to detect high-flux proton beams. Each curve represents the average energy deposited per proton in a single RCF layer using SRIM stopping power tables with an LET correction<sup>30</sup> applied. Bottom: corresponding dose deposited in RCF stack. Visibility of dose variations in HD-V2 (circles), MD-V3 (triangles), and EBT3 (squares) is indicated by the variation in color.

by scaling down the proton energy by a factor of 3. In previous studies comparing the results of 2D and 3D simulations of laser-jet interactions with experimental data, we have found that this scaling factor typically allows for a reasonable extrapolation of the 2D proton spectrum to 3D.<sup>39</sup> Similar scaling factors were observed by other groups.<sup>40</sup> The proton spectrum was then normalized to ensure a number of protons of  $2.3 \times 10^{13}$  protons/MeV/sr consistent with the typical conversion efficiency and half-angle divergence for TNSA (10%, 20° at 1 MeV) and is shown in the top plot in Fig. 6. A simulated proton spectrum can be used for the initial stack design followed by iterative improvements with experimental data.

The resulting RCF stack for detection up to 85 MeV, which maximizes the visibility consists of  $1 \times (13\ \mu\text{m Al} + \text{HD-V2}) + 7 \times (100\ \mu\text{m Al} + \text{HD-V2}) + 1 \times (100\ \mu\text{m Al} + \text{MD-V3}) + 6 \times (150\ \mu\text{m Cu} + \text{MD-V3}) + 1 \times (500\ \mu\text{m Cu} + \text{MD-V3}) + 12 \times (500\ \mu\text{m Cu} + \text{EBT3})$ . The energy deposition profiles for each RCF layer are shown in the middle row of Fig. 6. Stopping power tables from SRIM are used to determine the energy deposited in each layer, and an LET correction is applied.<sup>30</sup> The resulting dose is computed for a typical distance of 55 mm to the front of the RCF stack. Since the thickness of large-energy-range RCF stacks is non-negligible, the distance is updated for each successive layer.

## V. CONCLUSION

In this work, we have presented extended-dose calibrations of GafChromic EBT3, MD-V3, and HD-V2 radiochromic films and have defined optimal dose ranges for each film type based on visibility. Robust film calibrations are needed when using radiochromic film stacks to record quantitative proton spectra produced by petawatt-class short-pulse lasers. Until now, research in laser-produced ion beams has predominantly focused on smooth, laminar beams. Laser and target technology<sup>41,42</sup> or the use of pulsed high-field solenoid lenses<sup>43</sup> has recently led to tightly focused or structured ion beams. The deflections and perturbations observed on the ion beam can contain information about the ultra-fast plasma processes occurring in the interaction. It is therefore necessary to fully resolve these features, as a function of energy, to gain insight into the temporal and spatial scales of instabilities such as Weibel-type instabilities.<sup>39,44</sup> These calibration curves, used in conjunction with our visibility analysis, will allow the design of film-based large-angle sampling of high-flux ion beams or laser-driven ion beams with high flux zones (i.e., caustics<sup>45</sup>) formed by >100 MG magnetic fields produced in petawatt laser–plasma interactions.<sup>46</sup>

## SUPPLEMENTARY MATERIAL

See the [supplementary material](#) for the calibrated optical density response curve for the Epson Perfection V750 Pro used in this study.

## ACKNOWLEDGMENTS

The authors gratefully acknowledge the technical support provided by BC Cancer—Victoria, and the Medical Isotope and Cyclotron Facility (MICF) at the University of Alberta as well as R. Fedosejevs (University of Alberta) for his help with the cyclotron measurements. This work was supported by the U.S. DOE Office of Science, Fusion Energy Science under FWP No. 100182, FWP No. 100331, and Contract No. DE-SC0019167: the LaserNetUS initiative at the Texas Petawatt Laser facility. This material is based upon work supported in part by the National Science Foundation under Grant No. 1632708. C.B.C. acknowledges partial support from the Natural Sciences and Engineering Research Council of Canada (NSERC). G.D.G. was supported by the National Science Foundation Graduate Research Fellowship Program under Grant No. DGE-1656518. Simulations were run on Cori (NERSC) through an ALCC award.

## DATA AVAILABILITY

The data that support the findings of this study are available from the corresponding author upon reasonable request.

## REFERENCES

- <sup>1</sup>M. Roth, T. E. Cowan, M. H. Key, S. P. Hatchett, C. Brown, W. Fountain, J. Johnson, D. M. Pennington, R. A. Snavely, S. C. Wilks, K. Yasuike, H. Ruhl, F. Pegoraro, S. V. Bulanov, E. M. Campbell, M. D. Perry, and H. Powell, *Phys. Rev. Lett.* **86**, 436 (2001).
- <sup>2</sup>J. C. Fernández, J. J. Honrubia, B. J. Albright, K. A. Flippo, D. C. Gautier, B. M. Hegelich, M. J. Schmitt, M. Temporal, and L. Yin, *Nucl. Fusion* **49**, 065004 (2009).
- <sup>3</sup>S. V. Bulanov, T. Z. Esirkepov, V. S. Khoroshkov, A. V. Kuznetsov, and F. Pegoraro, *Phys. Lett. A* **299**, 240 (2002).

- <sup>4</sup>V. Malka, S. Fritzler, E. Lefebvre, E. d'Humières, R. Ferrand, G. Grillon, C. Albaret, S. Meyroneinc, J.-P. Chambaret, A. Antonetti, and D. Hulin, *Med. Phys.* **31**, 1587 (2004).
- <sup>5</sup>T. Tajima, D. Habs, and X. Yan, *Reviews of Accelerator Science and Technology*, Medical Applications of Accelerators Vol. 2 (World Scientific, 2009), p. 201.
- <sup>6</sup>E. S. Diffenderfer, I. I. Verginadis, M. M. Kim, K. Shoniyozov, A. Velalopoulou, D. Goia, M. Putt, S. Hagan, S. Avery, K. Teo, W. Zou, A. Lin, S. Swisher-McClure, C. Koch, A. R. Kennedy, A. Minn, A. Maity, T. M. Busch, L. Dong, C. Koumenis, J. Metz, and K. A. Cengel, *Int. J. Radiat. Oncol., Biol., Phys.* **106**, 440 (2020).
- <sup>7</sup>N. Esplen, M. Mendonca, and M. Bazalova-Carter, "Physics and biology of ultra-high dose-rate (FLASH) radiotherapy: a topical review," *Phys. Med. Biol.* (to be published) (2020).
- <sup>8</sup>M. Borghesi, D. H. Campbell, A. Schiavi, M. G. Haines, O. Willi, A. J. Mackinnon, P. Patel, L. A. Gizzi, M. Galimberti, R. J. Clarke, F. Pegoraro, H. Ruhl, and S. Bulanov, *Phys. Plasmas* **9**, 2214 (2002).
- <sup>9</sup>L. Romagnani, J. Fuchs, M. Borghesi, P. Antici, P. Audebert, F. Ceccherini, T. Cowan, T. Grismayer, S. Kar, A. Macchi, P. Mora, G. Pretzler, A. Schiavi, T. Toncian, and O. Willi, *Phys. Rev. Lett.* **95**, 195001 (2005).
- <sup>10</sup>M. Gauthier, S. N. Chen, A. Levy, P. Audebert, C. Blancard, T. Ceccotti, M. Cerchez, D. Doria, V. Floquet, E. Lamour, C. Peth, L. Romagnani, J.-P. Rozet, M. Scheinder, R. Shepherd, T. Toncian, D. Vernhet, O. Willi, M. Borghesi, G. Faussurier, and J. Fuchs, *Phys. Rev. Lett.* **110**, 135003 (2013).
- <sup>11</sup>A. B. Zylstra, J. A. Frenje, P. E. Grabowski, C. K. Li, G. W. Collins, P. Fitzsimmons, S. Glenzer, F. Graziani, S. B. Hansen, S. X. Hu, M. G. Johnson, P. Keiter, H. Reynolds, J. R. Rygg, F. H. Séguin, and R. D. Petrasso, *Phys. Rev. Lett.* **114**, 215002 (2015).
- <sup>12</sup>R. A. Snavely, M. H. Key, S. P. Hatchett, T. E. Cowan, M. Roth, T. W. Phillips, M. A. Stoyer, E. A. Henry, T. C. Sangster, M. S. Singh, S. C. Wilks, A. MacKinnon, A. Offenberger, D. M. Pennington, K. Yasuike, A. B. Langdon, B. F. Lasinski, J. Johnson, M. D. Perry, and E. M. Campbell, *Phys. Rev. Lett.* **85**, 2945 (2000).
- <sup>13</sup>P. Patel, A. Mackinnon, M. Key, T. Cowan, M. Foord, M. Allen, D. Price, H. Ruhl, P. Springer, and R. Stephens, *Phys. Rev. Lett.* **91**, 125004 (2003).
- <sup>14</sup>A. Pelka, G. Gregori, D. O. Gericke, J. Vorberger, S. H. Glenzer, M. M. Günther, K. Harres, R. Heathcote, A. L. Kritcher, N. L. Kugland, B. Li, M. Makita, J. Mithen, D. Neely, C. Niemann, A. Otten, D. Riley, G. Schaumann, M. Schollmeier, A. Tauschwitz, and M. Roth, *Phys. Rev. Lett.* **105**, 265701 (2010).
- <sup>15</sup>A. J. Mackinnon, P. K. Patel, R. P. Town, M. J. Edwards, T. Phillips, S. C. Lerner, D. W. Price, D. Hicks, M. H. Key, S. Hatchett, S. C. Wilks, M. Borghesi, L. Romagnani, S. Kar, T. Toncian, G. Pretzler, O. Willi, M. Koenig, E. Martinolli, S. Lepape, A. Benuzzi-Mounaix, P. Audebert, J. C. Gauthier, J. King, R. Snavely, R. R. Freeman, and T. Boehlly, *Rev. Sci. Instrum.* **75**, 3531 (2004).
- <sup>16</sup>M. Borghesi, A. Schiavi, D. H. Campbell, M. G. Haines, O. Willi, A. J. Mackinnon, P. Patel, M. Galimberti, and L. A. Gizzi, *Rev. Sci. Instrum.* **74**, 1688 (2003).
- <sup>17</sup>E. Breschi, M. Borghesi, M. Galimberti, D. Giulietti, L. A. Gizzi, and L. Romagnani, *Nucl. Instrum. Methods Phys. Res., Sect. A* **522**, 190 (2004).
- <sup>18</sup>D. S. Hey, M. H. Key, A. J. Mackinnon, A. G. MacPhee, P. K. Patel, R. R. Freeman, L. D. Van Woerkom, and C. M. Castaneda, *Rev. Sci. Instrum.* **79**, 053501 (2008).
- <sup>19</sup>F. Nürnberg, M. Schollmeier, E. Brambrink, A. Blažević, D. C. Carroll, K. Flippo, D. C. Gautier, M. Geißel, K. Harres, B. M. Hegelich, O. Lundh, K. Markey, P. McKenna, D. Neely, J. Schreiber, and M. Roth, *Rev. Sci. Instrum.* **80**, 033301 (2009).
- <sup>20</sup>D. Kirby, S. Green, F. Fiorini, D. Parker, L. Romagnani, D. Doria, S. Kar, C. Lewis, M. Borghesi, H. Palmans *et al.*, *Laser Part. Beams* **29**, 231 (2011).
- <sup>21</sup>P. R. Bolton, M. Borghesi, C. Brenner, D. C. Carroll, C. De Martinis, F. Fiorini, A. Flacco, V. Floquet, J. Fuchs, P. Gallegos, D. Giove, J. S. Green, S. Green, B. Jones, D. Kirby, P. McKenna, D. Neely, F. Nuesslin, R. Prasad, S. Reinhardt, M. Roth, U. Schramm, G. G. Scott, S. Ter-Avetisyan, M. Tolley, G. Turchetti, and J. J. Wilkens, *Phys. Med.* **30**, 255 (2014).
- <sup>22</sup>M. Bazalova-Carter, M. Liu, B. Palma, M. Dunning, D. McCormick, E. Hemsing, J. Nelson, K. Jobe, E. Colby, A. C. Koong, S. Tantawi, V. Dolgashev, P. G. Maxim, and B. W. Loo, Jr., *Med. Phys.* **42**, 1606 (2015).

- <sup>23</sup>P. R. Almond, P. J. Biggs, B. M. Coursey, W. F. Hanson, M. S. Huq, R. Nath, and D. W. O. Rogers, *Med. Phys.* **26**, 1847 (1999).
- <sup>24</sup>Y. Feng, H. F. Tiedje, K. Gagnon, and R. Fedosejevs, *Rev. Sci. Instrum.* **89**, 043511 (2018).
- <sup>25</sup>S. Devic, J. Seuntjens, E. Sham, E. B. Podgorsak, C. R. Schmidtlein, A. S. Kirov, and C. G. Soares, *Med. Phys.* **32**, 2245 (2005).
- <sup>26</sup>S. Devic, *Phys. Med.* **27**, 122 (2011).
- <sup>27</sup>S. N. Chen, M. Gauthier, M. Bazalova-Carter, S. Bolanos, S. Glenzer, R. Riquier, G. Revet, P. Antici, A. Morabito, A. Propp, M. Starodubtsev, and J. Fuchs, *Rev. Sci. Instrum.* **87**, 073301 (2016).
- <sup>28</sup>X. H. Xu, Q. Liao, M. J. Wu, Y. X. Geng, D. Y. Li, J. G. Zhu, C. C. Li, R. H. Hu, Y. R. Shou, Y. H. Chen, H. Y. Lu, W. J. Ma, Y. Y. Zhao, K. Zhu, C. Lin, and X. Q. Yan, *Rev. Sci. Instrum.* **90**, 033306 (2019).
- <sup>29</sup>J. H. Bin, Q. Ji, P. A. Seidl, D. Raftrey, S. Steinke, A. Persaud, K. Nakamura, A. Gonsalves, W. P. Leemans, and T. Schenkel, *Rev. Sci. Instrum.* **90**, 053301 (2019).
- <sup>30</sup>M. Schollmeier, M. Geissel, A. B. Sefkow, and K. A. Flippo, *Rev. Sci. Instrum.* **85**, 043305 (2014).
- <sup>31</sup>M. Vadrucchi, G. Esposito, C. Ronsivalle, R. Cherubini, F. Marracino, R. M. Montetereali, L. Picardi, M. Piccinini, M. Pimpinella, M. A. Vincenti, and C. De Angelis, *Med. Phys.* **42**, 4678 (2015).
- <sup>32</sup>M. Najafi, G. Geraily, A. Shirazi, M. Esfahani, and J. Teimouri, *Med. Dosim.* **42**, 159 (2017).
- <sup>33</sup>S. Aldelaijan and S. Devic, *Phys. Med.* **49**, 112 (2018).
- <sup>34</sup>A. Yogo, K. Mima, N. Iwata, S. Tosaki, A. Morace, Y. Arikawa, S. Fujioka, T. Johzaki, Y. Sentoku, H. Nishimura, A. Sagisaka, K. Matsuo, N. Kamit-sukasa, S. Kojima, H. Nagatomo, M. Nakai, H. Shiraga, M. Murakami, S. Tokita, J. Kawanaka, N. Miyanaga, K. Yamanoi, T. Norimatsu, H. Sakagami, S. V. Bulanov, K. Kondo, and H. Azechi, *Sci. Rep.* **7**, 42451 (2017).
- <sup>35</sup>D. Mariscal, T. Ma, S. C. Wilks, A. J. Kemp, G. J. Williams, P. Michel, H. Chen, P. K. Patel, B. A. Remington, M. Bowers, L. Pelz, M. R. Hermann, W. Hsing, D. Martinez, R. Sigurdsson, M. Prantil, A. Conder, J. Lawson, M. Hamamoto, P. Di Nicola, C. Widmayer, D. Homoelle, R. Lowe-Webb, S. Herriot, W. Williams, D. Alessi, D. Kalantar, R. Zacharias, C. Haefner, N. Thompson, T. Zobrist, D. Lord, N. Hash, A. Pak, N. Lemos, M. Tabak, C. McGuffey, J. Kim, F. N. Beg, M. S. Wei, P. Norreys, A. Morace, N. Iwata, Y. Sentoku, D. Neely, G. G. Scott, and K. Flippo, *Phys. Plasmas* **26**, 043110 (2019).
- <sup>36</sup>F. Fiuza, M. Marti, R. A. Fonseca, L. O. Silva, J. Tonge, J. May, and W. B. Mori, *Plasma Phys. Controlled Fusion* **53**, 074004 (2011).
- <sup>37</sup>M. Gauthier, J. B. Kim, C. B. Curry, B. Aurand, E. J. Gamboa, S. Göde, C. Goyon, A. Hazi, S. Kerr, A. Pak, A. Propp, B. Ramakrishna, J. Ruby, O. Willi, G. J. Williams, C. Rödel, and S. H. Glenzer, *Rev. Sci. Instrum.* **87**, 11D827 (2016).
- <sup>38</sup>L. Obst, S. Göde, M. Rehwald, F.-E. Brack, J. Branco, S. Bock, M. Bussmann, T. E. Cowan, C. B. Curry, F. Fiuza, M. Gauthier, R. Gebhardt, U. Helbig, A. Huebl, U. Hübner, A. Irman, L. Kazak, J. B. Kim, T. Kluge, S. Kraft, M. Loeser, J. Metzkes, R. Mishra, C. Rödel, H.-P. Schlenvoigt, M. Siebold, J. Tiggesbäumker, S. Wolter, T. Ziegler, U. Schramm, S. H. Glenzer, and K. Zeil, *Sci. Rep.* **7**, 10248 (2017).
- <sup>39</sup>S. Göde, C. Rödel, K. Zeil, R. Mishra, M. Gauthier, F.-E. Brack, T. Kluge, M. J. MacDonald, J. Metzkes, L. Obst, M. Rehwald, C. Ruyer, H.-P. Schlenvoigt, W. Schumaker, P. Sommer, T. E. Cowan, U. Schramm, S. Glenzer, and F. Fiuza, *Phys. Rev. Lett.* **118**, 194801 (2017).
- <sup>40</sup>K. D. Xiao, C. T. Zhou, K. Jiang, Y. C. Yang, R. Li, H. Zhang, B. Qiao, T. W. Huang, J. M. Cao, T. X. Cai, M. Y. Yu, S. C. Ruan, and X. T. He, *Phys. Plasmas* **25**, 023103 (2018).
- <sup>41</sup>L. Obst-Huebl, T. Ziegler, F.-E. Brack, J. Branco, M. Bussmann, T. E. Cowan, C. B. Curry, F. Fiuza, M. Garten, M. Gauthier, S. Göde, S. H. Glenzer, A. Huebl, A. Irman, J. B. Kim, T. Kluge, S. D. Kraft, F. Kroll, J. Metzkes-Ng, R. Pausch, I. Prencipe, M. Rehwald, C. Roedel, H.-P. Schlenvoigt, U. Schramm, and K. Zeil, *Nat. Commun.* **9**, 5292 (2018).
- <sup>42</sup>S. Kar, H. Ahmed, R. Prasad, M. Cerchez, S. Brauckmann, B. Aurand, G. Cantono, P. Hadjisolomou, C. L. S. Lewis, A. Macchi, G. Nersisyan, A. P. L. Robinson, A. M. Schroer, M. Swantusch, M. Zepf, O. Willi, and M. Borghesi, *Nat. Commun.* **7**, 10792 (2016).
- <sup>43</sup>F.-E. Brack, F. Kroll, L. Gaus, C. Bernert, E. Beyreuther, T. E. Cowan, L. Karsch, S. Kraft, L. A. Kunz-Schughart, E. Lessmann, J. Metzkes-Ng, L. Obst-Huebl, J. Pawelke, M. Rehwald, H.-P. Schlenvoigt, U. Schramm, M. Sobiella, E. R. Szabó, T. Ziegler, and K. Zeil, *Sci. Rep.* **10**, 9118 (2020).
- <sup>44</sup>C. Ruyer, S. Bolaños, B. Albertazzi, S. N. Chen, P. Antici, J. Böker, V. Dervieux, L. Lancia, M. Nakatsutsumi, L. Romagnani, R. Shepherd, M. Swantusch, M. Borghesi, O. Willi, H. Pépin, M. Starodubtsev, M. Grech, C. Riconda, L. Gremillet, and J. Fuchs, *Nat. Phys.* **16**, 983–988 (2020).
- <sup>45</sup>N. L. Kugland, D. D. Ryutov, C. Plechaty, J. S. Ross, and H.-S. Park, *Rev. Sci. Instrum.* **83**, 101301 (2012).
- <sup>46</sup>M. Nakatsutsumi, Y. Sentoku, A. Korzhimanov, S. N. Chen, S. Buffechoux, A. Kon, B. Atherton, P. Audebert, M. Geissel, L. Hurd, M. Kimmel, P. Rambo, M. Schollmeier, J. Schwarz, M. Starodubtsev, L. Gremillet, R. Kodama, and J. Fuchs, *Nat. Commun.* **9**, 280 (2018).